Università di Genova

Scuola Politecnica

DIME

Dipartimento di Ingegneria Meccanica, Energetica

Gestionale e dei Trasporti

Tesi di laurea triennale in Ingegneria Meccanica

-

Correlation between roughness and turbulence according to the homogenization theory

Allievo

Marco Sgambelluri

Supervisore
Prof. Alessandro Bottaro

Co-Supervisore
Dr. Essam Nabil Ahmed, Dr. Giulia Innocenti

Luglio 2025

Alla mia famiglia, che mi ha sostenuto e permesso di raggiungere quest'obiettivo importante,
al mio grande amore, Tania, che mi ha resto tutto più semplice e possibile,
ai miei compagni di università, che mi hanno accompagnato in questo percorso,
a chi mi è stato vicino, Grazie.

M. S.

Abstract

In this work, we explore the correlation between wall roughness and turbulent flow behavior through the framework of asymptotic homogenization theory. The goal is to derive effective, non-empirical boundary conditions that relate the influence of microscale surface texture on macroscopic flow characteristics. After reviewing the theoretical foundations of turbulence and the impact of rough surfaces on velocity profiles, we employ a multiscale upscaling approach to extract the so-called slip length and interfacial permeability coefficients, which appear in the homogenized boundary conditions.

A numerical simulation is carried out using STAR-CCM+ to solve a steady, three-dimensional laminar flow over a representative rough surface composed of hemispherical cavities. From the dimensionless velocity and pressure fields, the slip coefficient in the streamwise direction ($\lambda_x = 0.1034$) and the interfacial permeability ($K_{xy}^{itf} = 0.0084$) are extracted.

These coefficients serve as effective parameters that describe how surface texture alters flow behavior and may be used to simplify future simulations or improve surface design. The results validate the asymptotic framework and suggest promising directions for future work, including the implementation of Direct Numerical Simulation (DNS) and the investigation of alternative roughness geometries such as hexagonal packing.

Contents

Symbology

Symbols

Re	Reynolds number
$\overline{u}$	Time average velocity
u'	Instantaneous velocity variation from the average
T	Period
t	Time
x	Stream direction
y	Normal-wall direction
z	Span direction
u	Stream velocity component
v	Normal-wall velocity component
w	Span velocity component
ρ	Density
p	Pressure
ν	Kinematic viscosity
μ	Dynamic viscosity
τ_{Re}	Reynolds shear stress
τ_v	Viscous stress
τ_T	Total shear stress

τ_w	Wall shear stress
ζ	Dimensionless parameter
u^+	Dimensionless wall velocity
y^+	Dimensionless ordinate
δ	Thickness of the boundary layer
κ	Von Karman constant
B, C	Experimental constants
U^+	Logarithmic velocity distribution
k	Sand grain roughness height
k_s	Equivalent sand grain roughness height
ΔU^+	Roughness function
k_a	Mean roughness height
k_q	Root mean square height
k_t	Maximum peak to valley height
k_z	Average peak to valley height
ES	Effective slope
λ	Solidity
k_{sk}	Skewness
k_u	Kurtosis
PDF	Probability density function
m_θ	θth moments of the PDF

DNS	Direct numerical simulation
l	Microscopic lenght scale
L	Macroscopic lenght scale
ϵ	Lenghts ratio
$\mathcal{R}$	Microscopic Reynolds number
$\mathbf{S}$	Traction vector

1 Introduction

Fluids, in most cases of technical interest, have a turbulent flow and this is a complex phenomenon that needs to be studied. It occurs when the Reynolds number is above approximately 4000; since *Re* is the ratio between the inertial and viscous forces, it means that we are in situations where the speed or density of the fluid is high. Both cases are extremely common if we think for example at means of air, land and naval transport, but not only of course.
One of the topics that arouse greatest interest in the study of turbulent motion concerns the factors that generate friction and energy losses caused by it and how to reduce them. In this paper, we discuss the link between the roughness of the surfaces and the speed of the fluid, trying to find an analytical law that can allow us to predict how much it can influence the fluid velocity, without having to resort to empirical results.
Each surface has its own roughness which can be superficial, when intrinsic to the material of which it is made (microscopic scale), or due to singular asperities such as screws or bolts, for example necessary for fixing "smooth" panels (macroscopic scale). In particular, for the first case, surface texture, also known as surface finish and surface morphology, comprises a series of geometrical irregularities that are randomly or uniformly extended over a smooth surface. As you will see later, the problem is to make the effects of each individual surface comparable and that their evaluation takes place in an analytical and therefore repeatable way. To do this, every real surface is traced back to an ideal model that causes the same effects as it. Nowadays, this occurs through a large number of empirical correlations obtained from various studies carried out.

2 Generalities on Turbulent Flow

Turbulent flow is a common state of fluid motion interested by continuous and random fluctuations of all the quantities representing the motion itself. It is characterized by the presence of vortices that contribute to the exchange of momentum and energy between the various areas of the flow field, with consequent mixing of fluid properties; this makes the state of motion three-dimensional and time dependent. Because of this, also nowadays there is no general solution to the Navier-Stokes equations about turbulent flow of an incompressible, Newtonian, continuum fluid, but we have different ways to study it. The most common analytical treatment is represented by a time-averaged approach (also called as Reynolds-averaged approach) that assumes turbulence as a statistical phenomena. It is known that, choosing a sufficiently long time interval, the temporal average value of velocity (equal for other properties) is stationary; this allows us to express istantaneous velocity as the sum of the time average value $\bar{u}$ and the instantaneous deviation from the average u', called agitation component:

$$u = \bar{u} + u' \tag{2.1}$$

where

$$\bar{u} = \lim_{T \to +\infty} \frac{1}{T} \int_{t_0}^{t_0+T} u(\mathbf{x}, t) dt \tag{2.2}$$

and

$$\bar{u'} = 0 \tag{2.3}$$

but the moment is not zero

$$\overline{u'^2} = \lim_{T \to +\infty} \frac{1}{T} \int_{t_0}^{t_0+T} (u - \bar{u})^2 dt \tag{2.4}$$

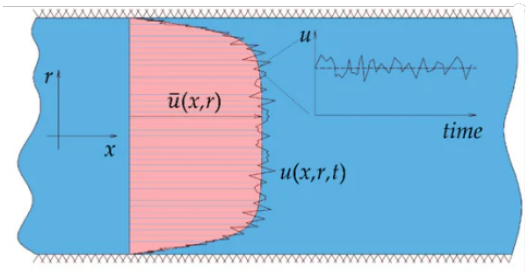

Figure 2.1: Instantaneous and mean velocity profiles in fully-developed channel flow [1].

The agitation components represent the chaotic fluctuations of fluid particles which they comport pressure and energy losses in the fluid path. That means that there are other shear stresses components due to it, add to viscous frictions effects; these are the Reynolds stresses [2, 3].

2.1 The Reynolds Stresses

Considering a fluid particle immersed in a turbulent flow field, due to the agitation component of the velocity in normal direction to the surface, it will move away from there, passing from slower area dA to a faster one. So, the slower particle has a mass flow rate ($\rho v' dA$); arriving in a faster zone of fluid, it will increase his velocity by u' and the particle receives from the faster fluid a flow rate, in direction of motion and in units of time, as $(\rho v' dA)u'$. This quantity also represent the flow rate decrease of fluid inside dA.
By Newton's second law, the force acting on a mass in a certain direction is equal to the change in velocity of momentum in the same direction; so the force acting in the direction of motion on a fluid element inside da, due to the passage of fluid particles through da and the consequent change in momentum is equal to $(\rho v' dA)(-u') = -\rho v' u' dA$. Dividing this shear force by area dA where it acts, we obtain what we can consider an instantaneous turbulent shear stress, also called Reynolds shear stress, expressible as:

$$\tau_{Re} = \rho \overline{u'v'} \tag{2.5}$$

where $\overline{u'v'}$ is the time average of the product of the agitation components u' and v'. Although any agitation component time averaged is zero, the time average of the product is not, as previously stated (2.4) [2].

2.2 Velocity profile on a smooth flat surface

Here we consider fully developed, turbulent, two-dimensional flow (x,y). This means that the flow is statistically stationary and homogeneous in the downstream direction; hence $\frac{\partial u}{\partial x} = 0$. Due to no-slip condition the velocity flow field on the surface is $\overline{u} = \overline{v} = \overline{w} = 0$ (time average values) and $u' = v' = w' = 0$ (agitation components), where the letters u, v, w respectively refer to the velocity components along the reference x,y,z directions [3].

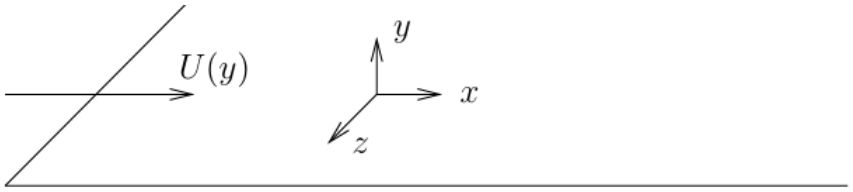

Figure 2.2: Reference triad.

Since the flow is two-dimensional, $\overline{w} = 0$ everywhere, and $\overline{w'v'} = 0$. So, we have:

$$u = \overline{u}(y) + u'; \quad v = \overline{v}(y) + v' \tag{2.6}$$

From the continuity equation for time average values we obtain $\dfrac{\mathrm{d}v}{\mathrm{d}y} = 0$; considering no slip condition we can say that:

$$u = \overline{u}(y) + u'; \quad v = v' \tag{2.7}$$

From the mean flow Reynolds-averaged equations

$$0 = -\frac{1}{\rho}\frac{\partial p}{\partial x} - \frac{\partial \overline{u'v'}}{\partial y} + \nu\frac{\partial^2 \bar{u}}{\partial y^2} \tag{2.8}$$

$$0 = -\frac{1}{\rho}\frac{\partial p}{\partial y} - \frac{\partial \overline{v'}^2}{\partial y} \tag{2.9}$$

$$0 = -\frac{1}{\rho}\frac{\partial p}{\partial z} \tag{2.10}$$

Deriving for x the (2.9) (2.10) equations we have $\frac{\partial}{\partial y}\frac{\partial p}{\partial x} = 0$, $\frac{\partial}{\partial z}\frac{\partial p}{\partial x} = 0$, so we conclude that $\frac{\partial p}{\partial x}$ only depend on x.
Introducing viscous and Reynolds stresses

$$\tau_v = \mu\frac{\partial \bar{u}}{\partial y} \quad \tau_{Re} = -\rho\overline{u'v'} \tag{2.11}$$

and known that the total shear stress in given by the sum of Reynolds and viscous stresses, hence:

$$\tau_T = \mu\frac{\partial \bar{u}}{\partial y} - \rho\overline{u'v'} \tag{2.12}$$

substituting into equation (2.8)

$$\frac{\partial p}{\partial x} - \frac{\partial \tau_T}{\partial y} = 0 \tag{2.13}$$

And given that the first term is only a function of x and the second is only a function of y, for the equation to be satisfied, they can only be both constants.
The trend of τ_T in y is therefore linear and must also satisfy the boundary condition on the surface (when y=0, $\tau_T(0) = \tau_w$); using the pressure gradient at the wall $\frac{\mathrm{d}p_w}{\mathrm{d}x}$ we can obtain a more explicit form of the linear trend in y of τ_T:

$$\tau_T = \frac{\mathrm{d}p_w}{\mathrm{d}x}y + \tau_w \tag{2.14}$$

In laminar flow $\tau_T = \tau_v = \mu\frac{\partial \bar{U}}{\partial y}$ so, we could solve the equation for U and find Poiseuille's profile. For turbulent cases, it turns out to be more complex to solve because of the new unknown represented by τ_{Re}. In another way, we can proceed with the dimensional analysis:

$$\bar{u} = f\left(\frac{\tau_w}{\rho}, h, \nu, y\right) \tag{2.15}$$

It is defined with $u_\tau = \sqrt{\frac{\tau_w}{\rho}}$ a velocity scale, sometimes called as friction velocity, based on the wall shear stress. There are five quantities that are expressed by two mutually independent dimensions: L,T. By Π Buckhingham's theorem, there is therefore a relation between $(5-2) = 3$ quantity in dimensionless form, for example:

$$u^+ = f(\zeta, y^+) \tag{2.16}$$

where

- $u^+ = \frac{\bar{u}}{u_\tau}$: dimensionless wall velocity, equal to the ratio between the average velocity $\bar{u}$ and the friction velocity u_τ
- $\zeta = \frac{y}{h}$: dimensionless ordinate equal to the ratio between the ordinate and a geometric quantity of the channel h. This ordinate essentially represents an ordinate of the same order of magnitude as the actual dimensional one
- $y^+ = \frac{y}{\delta}$: dimensionless ordinate equal to the ratio between the ordinate and a viscous length, defined as $\delta = \frac{\nu}{u_\tau}$. This unit is commonly called **unit of the wall** and represents an ordinate capable of conveniently representing the areas of the field very close to the wall.

Considering the case where

$$\lim_{\zeta \to 0} f(\zeta, y^+) = f(y^+) \tag{2.17}$$

The (2.16) become

$$u^+ = f(y^+) \tag{2.18}$$

That is the complete similarity condition (independence of the h variable). The area where this relationship holds is called the inner layer. In particular, if within this area we are further close to the wall ($h \simeq 0$) we find that:

$$\tau_T \simeq \tau_w = \mu \frac{\mathrm{d}\bar{u}}{\mathrm{d}y} = cost \tag{2.19}$$

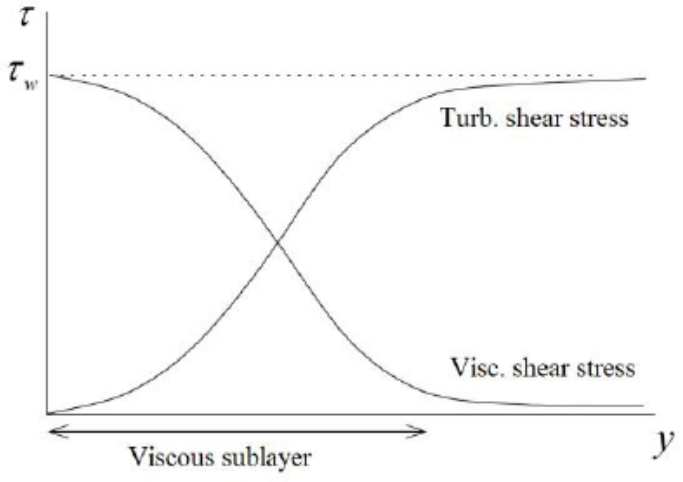

Figure 2.3: Viscous and turbulent shear stress distributions in the near-wall region.

At the wall the flow is dominated by viscous effects, then there is a buffer layer that precedes the overlap region, where turbulent effects are even more preponderant, up to the outer layer: moving away from the wall $-\overline{u'v'}$ becomes even more important and experiments have shown that it rapidly dominates momentum transport; this is what makes the prediction of turbulent boundary layers so difficult [3].
By Millikan's theory the overlap region is characterized by both limits $\zeta \to 0$, $y^+ \to \infty$ (which represents the inner and outer layer); calculating the derivatives $\frac{\mathrm{d}\bar{u}}{\mathrm{d}y}$ for both conditions:

$$\frac{\mathrm{d}\bar{u}}{\mathrm{d}y} = u_\tau \frac{\mathrm{d}f}{\mathrm{d}y^+}\frac{\mathrm{d}y^+}{\mathrm{d}y} = u_\tau \frac{u_\tau}{\nu}\frac{\mathrm{d}f}{\mathrm{d}y^+} \tag{2.20}$$

$$\frac{\mathrm{d}\bar{u}}{\mathrm{d}y} = u_\tau \frac{\mathrm{d}F}{\mathrm{d}\zeta}\frac{\mathrm{d}\zeta}{\mathrm{d}y} = u_\tau \frac{\mathrm{d}F}{\mathrm{d}\zeta}\frac{1}{h} \tag{2.21}$$

Multiplying for $\frac{y}{u_\tau}$ to render the equations dimensionless, we find the relation:

$$y^+ \frac{\mathrm{d}f}{\mathrm{d}y^+} = \zeta \frac{\mathrm{d}F}{\mathrm{d}\zeta} = cost = \frac{1}{\kappa} \tag{2.22}$$

where κ is Von Karman constant.
Focusing on the inner layer, integrating the previous equation, we found **the logarithmic law**:

$$U^+ = \frac{\bar{u}}{u_\tau} = \frac{1}{\kappa}\log y^+ + B \tag{2.23}$$

where ($\kappa \simeq 0.41$, $B \simeq 5.1$) are experimentally known constants. The log-law can explain velocity field in transition state between buffer layer and turbulent region, this mean that the velocity is congruent to the logarithm of the distance from the wall.

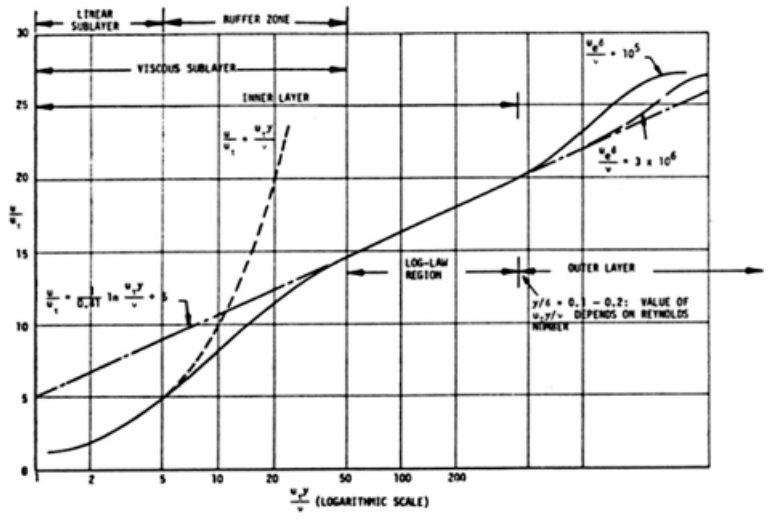

Figure 2.4: The log law represents satisfactorily the experimental data for entire inner layer, except for the closest zone at the wall where the trend is linear, as mentioned previously [2]

3 Roughness effects on turbulent flow and study approach

For a turbulent boundary layer over a smooth surface, a thin layer of laminar flow known as the viscous sublayer forms along the entire length of the surface. For the same flow over a rough surface, the roughness increases flow instability close to the wall which can lead to increased localised turbulence disrupting the viscous sublayer, thereby generating the roughness sublayer and affecting pressure drop and heat transfer. That translates in a drag increment that the surface offers at fluid passage.

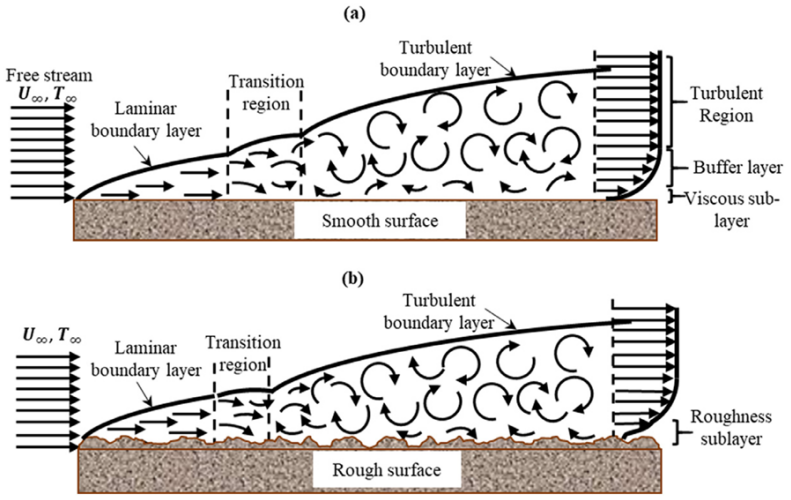

Figure 3.1: Boundary layer flows over (a) smooth and (b) rough surfaces [4]

Nikuradse investigated the effect of wall roughness on turbulent flows by measuring the pressure drop in pipes coated with uniform sand. His detailed experiments, insight into previous experiments, and correlation of his data set the stage for the prediction of rough-wall flows [5]. Based on Nikuradse's sand-grain experiments, Schlichting considered roughness effects on the flow by defining a roughness scale that reflects the effects of roughness characteristics on the flow. He considered the rough surface as a smooth one covered with a layer of uniform packed spheres, as dense as possible, where the diameter can be chosen to describe length scale; it is called sand grain roughness height (k). However, when the shape of roughness deviates from the sand-grain, a single parameter cannot describe the sand grain roughness anymore. In this case, geometrical parameters may be applied to characterize these type of surfaces. Therefore, an equivalent length scale was introduced by Colebrook and White so-called equivalent sand-grain roughness (k_s). The equivalent sand-grain roughness is an equivalent roughness height for irregular, and non-uniform rough surfaces that produce the same results as the uniform sand-grain of the Nikuradse for a fully rough flow regime.

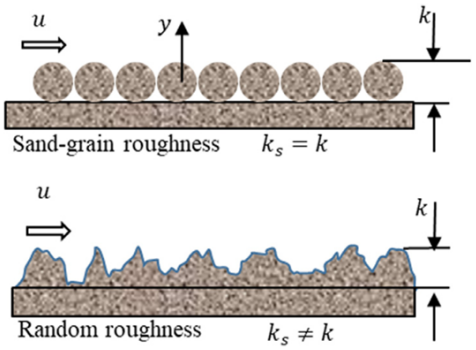

Figure 3.2: Equivalent sand-grain roughness [4]

Thus, the "roughness Reynolds number" (k_s^+) was defined as:

$$k_s^+ = \frac{k_s u_\tau}{\nu} \tag{3.1}$$

This parameter is introduced to account that wall roughness alters the law of the wall used to describe the viscous sublayer. It is also used to classify the flow into three regimes depending on equivalent sand grain roughness: $k_s^+ < 4$ for the hydraulically smooth regime, $4 \leq k_s^+ \leq 70$ for the transitionally rough regime and $k_s^+ > 70$ for the fully rough regime [6].

3.1 Velocity profile on a rough flat surface

Depending on the rough flow regime, the viscous sublayer could partially (in transitionally rough regimes) or completely (in fully rough regimes) be destroyed by roughness. However, according to wall similarity hypothesis, the effect of the roughness on the flow is limited to the roughness sublayer, and the outer layer remains unaffected. In the roughness sublayer, the flow is highly disturbed due to the large turbulence mixing caused by roughness elements.
Based on these observations, researchers have attempted to develop models for mean flow over surface roughness, based on the available models of smooth wall flows. Clauser studied the effect of the surface roughness on the mean velocity distribution and presented a method that has demonstrated to be robust and widely applied. He argued that the velocity profile in the viscous sublayer for rough surfaces follows a logarithmic pattern with a similar slope as for smooth surfaces. He also found that the sole impact of the roughness is a downward shift of the log-law profile as a function of the roughness Reynolds number. Clauser and Hama, each in an independent study, introduced a parameter called roughness function (ΔU^+) to emulate the effect of the velocity shift caused by surface roughness. They observed that it shifts the logarithmic profile downward, commensurate with ΔU^+, indicating a shortage in momentum compared to smooth walls; the velocity change is proportional to $\ln(k_s^+)$ and is independent of the distance of the wall.
Thus, Clauser proposed the logarithmic velocity distribution for turbulent flow over rough walls as follows:

$$U^+ = \frac{1}{\kappa} \ln y^+ + B - \Delta U^+ \tag{3.2}$$

where B is the smooth-wall constant and κ is von Karman constant. In this way he has shown that the roughness function ΔU^+ is a sole function of the roughness Reynolds number (k_s^+).
Hama performed an extensive experimental study and proposed the roughness function for fully rough flows as:

$$\Delta U^+ = \frac{1}{\kappa} \ln k_s^+ + B - C \tag{3.3}$$

where C should reach a constant value in the fully rough regime [4].

3.2 Equivalent sand-grain roughness parameters

As previously mentioned (3), equivalent sand-grain roughness k_s can be obtained starting from many geometric parameters. There is no consensus on which roughness parameter best describes a surface in relation to friction drag. Over the years, many studies have attempted to identify the most appropriate surface parameters; the following are the most widely used: mean roughness height (k_a), root mean square height (k_q), maximum peak to valley height (k_t), average peak to valley height (k_z), effective slope (ES), solidity (λ), skewness (k_{sk}) and kurtosis (k_u). However, none of these parameters universally applies to all types of surfaces to describe its roughness [7].
To determine mathematically some of these parameters, it is possible to use the Probability Density Function (PDF), which represents the probability of a point on the surface that has height equal to y:

$$\int_{-\infty}^{+\infty} p(y)dy = 1 \tag{3.4}$$

The shape of PDF provides useful information about surface's nature and can be evaluated by its moments. The central θth moment of the PDF with zero mean, m_θ, is defined as:

$$m_\theta = \int_{-\infty}^{+\infty} y^\theta p(y)dy \tag{3.5}$$

The roughness parameters can be defined as

$$k_q = \sqrt{m_2} \quad k_{sk} = m_3/m_2^{3/2} \quad k_u = m_4/m_2^4 \tag{3.6}$$

Effective Slope parameter was introduced by Napoli et al. to distinguish between roughness and waviness surface. It is defined as the average value of the magnitude of the slope of the roughness corrugation, written as:

$$ES = \frac{1}{l_x l_z} \int_0^l \int_0^{l_z} \left| \frac{\partial k(x,z)}{\partial x} \right| dxdz \tag{3.7}$$

where $k(x,z)$ is the roughness amplitude, while l_x and l_z are the sampling length in stream and span directions, respectively. Pyramid roughness and 2D wave-composite surfaces with an effective slope of approximately less than 0.35, do not

scale on the roughness height and are classified as wavy surfaces.
Solidity (λ) is defined as the ratio of the average roughness element spacing (ψ) to the effective slope roughness height (ES); a relation of ES = 2λ has been observed by several researchers [4].
According to [7] "*To effectively describe a rough surface, a combination of the three roughness categories, namely height, slope, and asymmetry, is considered to be the most appropriate approach to understanding the impact of these roughness parameters on a turbulent boundary layer (TBL) and to identify the specific parameters that influence turbulence statistics and drag coefficient.*"

3.3 Limitations of the Roughness Reynolds Number

Despite its popularity, the use of k_s^+ entails several conceptual and practical drawbacks, especially for complex or engineered surfaces.

- **Implicit reliance on empirical models**

  The definition of k_s^+ stems from Nikuradse's sand-grain experiments, characterised by uniform, closely packed spheres. Applying the same parameter to real, irregular textures assumes that a single scalar k_s can reproduce the same head loss, an assumption that is inherently empirical and often unjustified.

- **Ambiguity in determining k_s**

  There is no unique procedure to infer k_s from a given texture. Different geometric metrics (mean height k_a, rms height k_q, peak-to-valley height k_t, effective slope (ES), skewness, kurtosis, etc.) lead to different values. Consequently, distinct surfaces may share the same k_s yet generate different flow responses, and vice versa.

- **Validity restricted to the fully rough regime**

  Classical relations, such as Hama's roughness function

  $$\Delta U^+ = \frac{1}{\kappa} \ln k_s^+ + B - C,$$

  are valid only in the fully rough regime, where viscous effects near the wall are negligible. In the transitional range ($4 \lesssim k_s^+ \lesssim 70$), no single universal law exists, and case-specific calibration is usually required.

- **Inability to capture anisotropic or non-local effects**

  The parameter k_s^+ is a *scalar*. It cannot account for directional (anisotropic) textures, non-uniform distributions, multiscale features or three-dimensional interactions among roughness elements, all of which can markedly alter boundary-layer behaviour.

- **Unsuitability for modern engineered surfaces**

  Contemporary applications increasingly employ micro-textured, gradient, porous or super-hydrophobic coatings. For such surfaces, the notion of hydraulic

equivalence with a sand-grain layer is untenable, and k_s^+ fails to predict drag or heat-transfer variations accurately.

While k_s^+ remains a convenient classification tool for canonical roughness, its limitations motivate the search for alternative approaches. As shown in this thesis, *asymptotic homogenisation* offers a more robust framework: it replaces the real texture with non-empirical, wall-scale boundary conditions, such as slip lengths and interface permeabilities, directly derived from the surface geometry.

4 Asymptotic homogenization

Investigating how the microscale features of a surface, such as roughness, can alter the characteristics of the turbulent motion above it and consequently affect skin-friction drag or heat and mass transfer effectiveness, is important for both predictive and optimization purposes in various applications. The numerical complexity and high computational cost of resolving turbulent fields near and across surface micro-details pose a significant challenge. This is due to the diverse range of surface topographies encountered in practice, the computational expense of performing well-resolved direct numerical simulation (DNS) or large-eddy simulations, and the uncertainties and errors related to the numerical representation of rough surfaces or grain shapes and distributions.
Asymptotic multiscale homogenization theory provides a theoretical framework through which the rapidly varying properties of a heterogeneous surface (such as irregular, rough, lubricant-infused or porous surfaces) can be replaced with homogeneous upscaled parameters, such as Navier's slip length, which helps formulate effective boundary conditions, free of empirical coefficients, to be imposed at a hypothetical plane interface next to the actual textured boundary. This approach allows for the numerical study of the macroscale behavior of channel flow without the need to resolve flow details in the immediate vicinity of solid protrusions or grains, thereby reducing mesh requirements and computational costs.

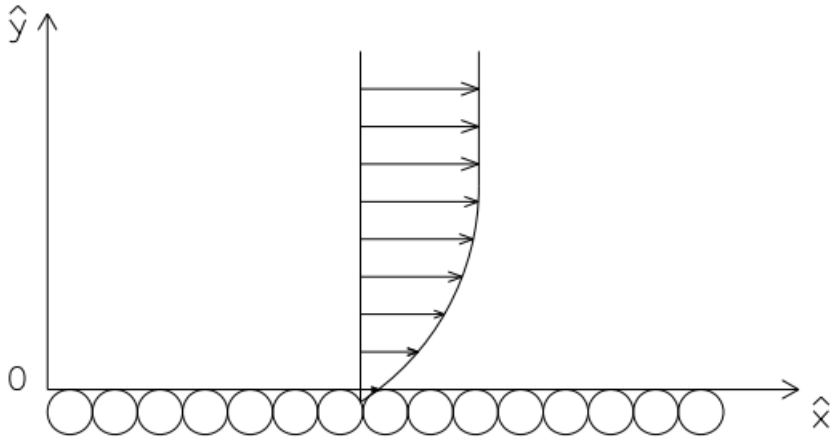

Figure 4.1: No-slip boundary condition on each individual grain

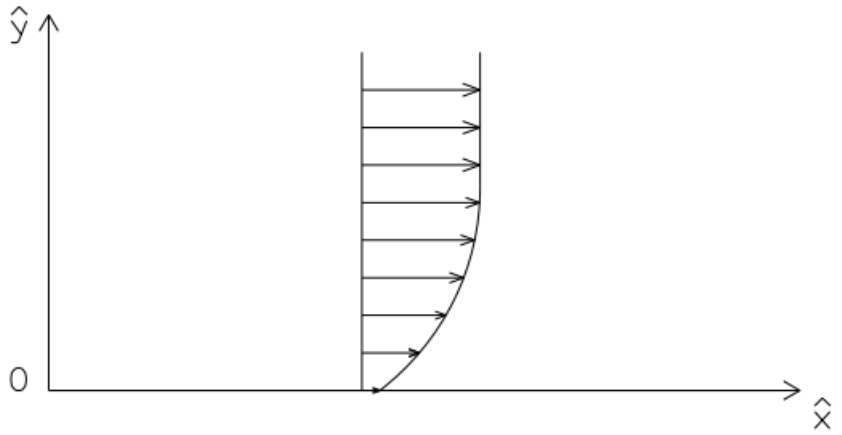

Figure 4.2: Effective boundary condition arising from homogenization

The validity of the asymptotic homogenization approach depends on the presence of well-separated scales. For instance, there must be a microscopic length scale (l) related to the periodicity of the surface texture and a macroscopic length scale (L), where $L \gg l$, related to the large-scale flow structures in the channel. This allows, by the definition of the small parameter $\epsilon = l/L \ll 1$, to find a solution manipulating the microscale problem by means of an asymptotic analysis up to the required order of accuracy, in terms of a ϵ [8].

4.1 Upscaling approach

Considering the turbulent flow of a viscous incompressible Newtonian fluid in a rough wall, the velocity components ($\hat{u}_1 = \hat{u}$; $\hat{u}_2 = \hat{v}$; $\hat{u}_3 = \hat{w}$) and pressure $\hat{p}$ are dependent variables to be evaluated over space ($\hat{x}_1 = \hat{x}$; $\hat{x}_2 = \hat{y}$; $\hat{x}_3 = \hat{z}$) and time $\hat{t}$ (afterword we will refer to macroscopic parameters with capital case letters and microscopic parameters with small case letters). The conservation equations governing the flows are the following:

$$\frac{\partial \hat{u}_i}{\partial \hat{x}_i} = 0; \tag{4.1}$$

$$\rho\left(\frac{\partial \hat{u}_i}{\partial \hat{t}} + \hat{u}_j \frac{\partial \hat{u}_i}{\partial \hat{x}_j}\right) = -\frac{\partial \hat{p}}{\partial \hat{x}_i} + \mu \frac{\partial^2 \hat{u}_i}{\partial \hat{x}_j^2} \tag{4.2}$$

with ρ and μ the fluid density and dynamic viscosity, respectively.
We now define the micro- and macro- characteristic length scales referring to near-surface flow and large-scale flow, respectively, as mentioned above:

Scales	Macro	Micro
Lenght	L	l
Velocity	$\hat{U}$	$\hat{u}$
Pressure	$\rho\hat{U}^2$	$\rho\hat{u}^2$
Time	$\frac{L}{\hat{U}}$	$\frac{l}{\hat{u}}$

Once the scales are defined, we need to normalize every parameter of the governing equations to find the dimensionless equations of the problem.

Macro:

$$X_i = \frac{\hat{X}_i}{L}; \quad U_i = \frac{\hat{U}_i}{\hat{U}}; \quad P = \frac{\hat{P}}{\rho\hat{U}^2}; \quad T = \frac{\hat{t}\,\hat{U}}{L} \tag{4.3}$$

The dimensionless continuity and momentum equations are, respectively:

$$\frac{\partial U_i}{\partial X_i} = 0; \tag{4.4}$$

$$\frac{\partial U_i}{\partial T} + U_j\frac{\partial U_i}{\partial X_j} = -\frac{\partial P}{\partial X_i} + \frac{1}{Re}\frac{\partial^2 U_i}{\partial X_j^2} \tag{4.5}$$

where $Re = (\rho\hat{U}L/\mu)$ is the Reynolds number of the macroscopic problem.

Micro:

$$x_i = \frac{\hat{x}_i}{l}; \quad u_i = \frac{\hat{u}_i}{\hat{u}}; \quad p = \frac{\hat{p}}{\rho\hat{u}^2}; \quad t = \frac{\hat{t}\,\hat{u}}{l} \tag{4.6}$$

The dimensionless continuity and momentum equations are, respectively:

$$\frac{\partial u_i}{\partial x_i} = 0; \tag{4.7}$$

$$\mathcal{R}\left(\frac{\partial u_i}{\partial t} + u_j\frac{\partial u_i}{\partial x_j}\right) = -\frac{\partial p}{\partial x_i} + \frac{\partial^2 u_i}{\partial x_j^2} \tag{4.8}$$

where $\mathcal{R} = (\rho\hat{u}l/\mu)$ is the Reynolds number of the microscopic problem.
The momentum equation (4.9) can be rewritten as follows, since $\mathcal{R} = \epsilon^2 Re$

$$\epsilon^2 Re\left(\frac{\partial u_i}{\partial t} + u_j\frac{\partial u_i}{\partial x_j}\right) = -\frac{\partial p}{\partial x_i} + \frac{\partial^2 u_i}{\partial x_j^2} \tag{4.9}$$

Next step is to define boundary condition of the problem:

- No-slip condition at the physical interface

$$u_i = 0 \tag{4.10}$$

- The virtual surface is defined at $\hat{x}_2 = \hat{y}_\infty$, and continuity of velocity and the traction vectors is applied there, so the matching conditions can be written as: continuity of velocity

$$u_i\Big|_{y=y_\infty} = \frac{1}{\epsilon} U_i\Big|_{Y=Y_\infty} \tag{4.11}$$

continuity of the components of the traction vector at the interface between the two regions

$$\begin{aligned}
\left(\frac{\partial u_1}{\partial x_2} + \frac{\partial u_2}{\partial x_1}\right)\Big|_{y=y_\infty} &= \left(\frac{\partial U_1}{\partial X_2} + \frac{\partial U_2}{\partial X_1}\right)\Big|_{Y=Y_\infty} = S_{12} \\
\left(-p + 2\frac{\partial u_2}{\partial x_2}\right)\Big|_{y=y_\infty} &= \left(-ReP + 2\frac{\partial U_2}{\partial X_2}\right)\Big|_{Y=Y_\infty} = S_{22} \\
\left(\frac{\partial u_3}{\partial x_2} + \frac{\partial u_2}{\partial x_3}\right)\Big|_{y=y_\infty} &= \left(\frac{\partial U_3}{\partial X_2} + \frac{\partial U_2}{\partial X_3}\right)\Big|_{Y=Y_\infty} = S_{32}.
\end{aligned} \tag{4.12}$$

4.2 Asymptotic analysis of microscale problem

An asymptotic analysis is then performed on the microscopic problem, which is reconstructed at different orders of the parameter ϵ. Each variable of the problem is expressed in the following form:

$$f = \epsilon^0 f^{(0)} + \epsilon^1 f^{(1)} + \epsilon^2 f^{(2)} + ... \tag{4.13}$$

Furthermore, the gradients are recast using the chain rule

$$\frac{\partial}{\partial x_i} \rightarrow \frac{\partial}{\partial x_i} + \epsilon \frac{\partial}{\partial X_i} \tag{4.14}$$

$$\frac{\partial^2}{\partial x_i^2} \rightarrow \frac{\partial^2}{\partial x_i^2} + \epsilon^2 \frac{\partial}{\partial X_i^2} + 2\epsilon \frac{\partial^2}{\partial x_i \partial X_i} \tag{4.15}$$

Asymptotic expressions are substituted in the equations governing the flow in the microscopic regions to reconstruct the microscale problems at different orders of ϵ. The resulting systems of equations for the interfacial region can be obtained by defining a description of the asymptotic expansions. So, the velocity components and pressure are expressed as follows:

$$\begin{cases}
u_i = \epsilon^0 u_i^{(0)} + \epsilon^1 u_i^{(1)} + O(\epsilon^2) \\
p = \epsilon^0 p^{(0)} + \epsilon^1 p^{(1)} + O(\epsilon^2)
\end{cases} \tag{4.16}$$

At first order, the continuity and momentum equations are as follows

$$\begin{cases}
\dfrac{\partial u_i^{(0)}}{\partial x_i} = 0 \\
-\dfrac{\partial p^{(0)}}{\partial x_i} + \dfrac{\partial^2 u_i^{(0)}}{\partial x_j^2} = 0
\end{cases} \tag{4.17}$$

Then the boundary condition at the physical interface becomes

$$u_i^{(0)} = 0 \tag{4.18}$$

and at the virtual surface;

$$\begin{aligned}
\left(\frac{\partial u_1^{(0)}}{\partial x_2} + \frac{\partial u_2^{(0)}}{\partial x_1}\right)\Bigg|_{y=y_\infty} &= S_{12} \\
\left(-p^{(0)} + 2\frac{\partial u_2^{(0)}}{\partial x_2}\right)\Bigg|_{y=y_\infty} &= S_{22} \\
\left(\frac{\partial u_3^{(0)}}{\partial x_2} + \frac{\partial u_2^{(0)}}{\partial x_3}\right)\Bigg|_{y=y_\infty} &= S_{32}
\end{aligned} \tag{4.19}$$

Where S_{12}, S_{22}, S_{32} are the components of the traction vector **S**, exerted on the surface at y_∞ by the external (macroscopic) fluid flow. Since the problem, defined by equations (4.17);(4.19) and (4.25);(4.28), is linear and driven by the traction vector **S**, a general solution to the problem can be expressed in the following form, rewriting the dependent variables as:

$$\begin{cases}
u_1^{(0)} = u_{11}^\dagger S_{12} + u_{12}^\dagger S_{22} + u_{13}^\dagger S_{32} \\
u_2^{(0)} = u_{21}^\dagger S_{12} + u_{22}^\dagger S_{22} + u_{23}^\dagger S_{32} \\
u_3^{(0)} = u_{31}^\dagger S_{12} + u_{32}^\dagger S_{22} + u_{33}^\dagger S_{32} \\
p^{(0)} = p_1^\dagger S_{12} + p_2^\dagger S_{22} + p_3^\dagger S_{32}
\end{cases} \tag{4.20}$$

where parameters marked with (†) are auxiliary variables.
In order to solve the problem, it is necessary to substitute every variable $u_i^{(0)}$ and $p^{(0)}$ in the dimensionless Navier-Stokes equations applying boundary conditions, this will give values for auxiliary variables:

$$\begin{cases}
\dfrac{\partial u_{ij}^\dagger}{\partial x_i} = 0; \\
-\dfrac{\partial p_j^\dagger}{\partial x_i} + \dfrac{\partial^2 u_{ij}^\dagger}{\partial x_j^2} = 0 \\
\left(-p_j^\dagger \delta_{i2} + \dfrac{\partial u_{ij}^\dagger}{\partial x_2} + \dfrac{\partial u_{2j}^\dagger}{\partial x_i}\right)\Bigg|_{y=y_\infty} = \delta_{ij}
\end{cases} \tag{4.21}$$

The solution of the problem at the first order, forcing it by S_{22} (j=2), is easily retrieved as described below:

$$\begin{cases}
\dfrac{\partial u_{12}^\dagger}{\partial x_2} + \dfrac{\partial u_{22}^\dagger}{\partial x_1} = 0 & (i = 1) \\
-p_2^\dagger + \dfrac{\partial u_{22}^\dagger}{\partial x_2} + \dfrac{\partial u_{22}^\dagger}{\partial x_2} = 1 & (i = 2) \\
\dfrac{\partial u_{32}^\dagger}{\partial x_2} + \dfrac{\partial u_{22}^\dagger}{\partial x_3} = 0 & (i = 3)
\end{cases} \tag{4.22}$$

so that

$$\begin{cases} u_{i2}^{\dagger} = 0 \\ p_2^{\dagger} = -1 \end{cases} \tag{4.23}$$

To second order, the equations governing the problem become:

$$\frac{\partial u_i^{(1)}}{\partial x_i} = -\frac{\partial u_i^{(0)}}{\partial X_i} \tag{4.24}$$

$$-\frac{\partial p^{(1)}}{\partial x_i} + \frac{\partial^2 u_i^{(1)}}{\partial u_j^2} = \frac{\partial p^{(0)}}{\partial X_i} - 2\frac{\partial^2 u_i^{(o)}}{\partial x_j \partial X_j} \tag{4.25}$$

where the third equation is written in expanded form

$$\left(\frac{\partial u_1^{(1)}}{\partial x_2} + \frac{\partial u_2^{(1)}}{\partial x_1}\right)_{y=y_\infty} = -\left(\frac{\partial u_1^{(0)}}{\partial X_2} + \frac{\partial u_2^{(0)}}{\partial X_1}\right)_{y=y_\infty} \tag{4.26}$$

$$\left(-p^{(1)} + 2\frac{\partial u_2^{(1)}}{\partial x_2}\right)_{y=y_\infty} = -2\frac{\partial u_2^{(0)}}{\partial X_2}\bigg|_{y=y_\infty} \tag{4.27}$$

$$\left(\frac{\partial u_3^{(1)}}{\partial x_2} + \frac{\partial u_2^{(1)}}{\partial x_3}\right)_{y=y_\infty} = -\left(\frac{\partial u_3^{(0)}}{\partial X_2} + \frac{\partial u_2^{(0)}}{\partial X_3}\right)_{y=y_\infty} \tag{4.28}$$

The generic forms hold:

$$\begin{cases} u_i^{(1)} = u_{ijk}^{\ddagger} \dfrac{\partial S_{j2}}{\partial X_k} \\ p_i^{(1)} = p_{jk}^{\ddagger} \dfrac{\partial S_{j2}}{\partial X_k} \end{cases} \tag{4.29}$$

Replacing generic forms in Continuity and Momentum equations, it lead to the generic solution:

$$\frac{\partial S_{j2}}{\partial X_k}\left(\frac{\partial u_{ijk}^{\ddagger}}{\partial x_i}\right) = \frac{\partial S_{j2}}{\partial X_k}\left(-u_{ij}^{\dagger}\delta_{ik}\right) \tag{4.30}$$

$$\frac{\partial S_{j2}}{\partial X_k}\left(-\frac{\partial p_{jk}^{\ddagger}}{\partial x_i} + \frac{\partial^2 u_{ijk}^{\ddagger}}{\partial x_i^2}\right) = \frac{\partial S_{j2}}{\partial X_k}\left(p_j^{\dagger}\delta_{ik} - 2\frac{\partial u_{ij}^{\dagger}}{\partial x_k}\right) \tag{4.31}$$

These are nine decoupled system, corresponding to j,k=1,2,3. The closure problems (4.21) and (4.31) are to be solved in a representative unit cell of the microscopic region, subject to periodicity of all dependent variables along x and z and to the boundary conditions $u_{ij}^{\dagger} = 0$ and $u_{ijk}^{\ddagger} = 0$ on the solid grains, which come from the no-slip condition [8].

4.3 Effective boundary conditions

Numerical solutions are sought for systems (4.21) and (4.31), with focus on the values of the fields at $x_2 = y_\infty$, since $u^\dagger_{ij}\Big|_{y_\infty}$ and $u^\ddagger_{ijk}\Big|_{y_\infty}$ are eventually the necessary coefficients to close the macroscopic effective boundary conditions of the velocity. These conditions result from matching the velocity vector at the fictitious interface between the channel-flow and the interfacial regions.

Finally, the upscaled conditions, second-order accurate in terms of ϵ, are expressed as:

$$U_i|_{Y=\infty} = \epsilon\, u_i^{(0)}(y_\infty) + \epsilon\, u_i^{(1)}(y_\infty) + O(\epsilon^3) = \epsilon\, u^\dagger_{ij}(y_\infty) S_{j2} + \epsilon^2\, u^\ddagger_{ijk}(y_\infty) \frac{\partial S_{j2}}{\partial X_k} + O(\epsilon^3) \quad (4.32)$$

The numerical procedure to solve the closure problems is similar to that followed by Naqvi & Bottaro [9] and Ahmed et al. [10] for porous media of either isotropic (such as spherical grains) or transversely isotropic microstructures in the $\hat{x} - \hat{z}$ plane (such as spanwise- or streamwise-elongated elements). We focus on the same parameters which do not vanish at the matching interface found in these references:

$$\begin{aligned}
u^\dagger_{11}(y_\infty) &= y_\infty + \lambda_x, \\
u^\dagger_{33}(y_\infty) &= y_\infty + \lambda_z, \\
-u^\ddagger_{211}(y_\infty) = u^\ddagger_{121}(y_\infty) &= 0.5\, y_\infty^2 + \lambda_x y_\infty + K^{itf}_{xy}, \\
-u^\ddagger_{233}(y_\infty) = u^\ddagger_{323}(y_\infty) &= 0.5\, y_\infty^2 + \lambda_z y_\infty + K^{itf}_{zy}, \\
u^\ddagger_{222}(y_\infty) &= K_{yy},
\end{aligned} \quad (4.33)$$

with λ_x and λ_z are the dimensionless Navier slip coefficients in the streamwise and spanwise directions, respectively;
K^{itf}_{xy} and K^{itf}_{zy} are the interface permeability coefficients and K_{yy} is an intrinsic permeability component. The novel contribution here is the incorporation of the effect of near-interface inertia on the microscale flow behavior, which renders the aforementioned parameters sensitive to the value of Re_λ.

It is convenient to set $y_\infty = 0$ in the fitting relations (4.33) and, hence, to extrapolate the solutions of the model coefficients to a matching interface located at the upper boundary of the surface corrugation, that is, the porous/free-fluid interface at $Y = 0$. Therefore, the values of the parameters $\lambda_x, \lambda_z, K^{itf}_{xy}, K^{itf}_{zy}$ and K_{yy} are sufficient to macroscopically mimic the presence of the permeable interface up to second-order accuracy, with the following effective boundary conditions on the $Y = 0$ plane:

$$U|_{Y=0} = \epsilon\, \lambda_x\, S_{12}|_{Y=0} + \epsilon^2\, K^{itf}_{xy}\, \frac{\partial S_{22}}{\partial X}\bigg|_{Y=0} + O(\epsilon^3), \quad (4.34)$$

$$V|_{Y=0} = -\epsilon^2\, K^{itf}_{xy}\, \frac{\partial S_{12}}{\partial X}\bigg|_{Y=0} - \epsilon^2\, K^{itf}_{zy}\, \frac{\partial S_{32}}{\partial Z}\bigg|_{Y=0} + \epsilon^2\, K_{yy}\, \frac{\partial S_{22}}{\partial Y}\bigg|_{Y=0} + O(\epsilon^3), \quad (4.35)$$

$$W|_{Y=0} = \epsilon\, \lambda_z\, S_{32}|_{Y=0} + \epsilon^2\, K^{itf}_{zy}\, \frac{\partial S_{22}}{\partial Z}\bigg|_{Y=0} + O(\epsilon^3). \quad (4.36)$$

In dimensional form, after extrapolating the boundary conditions from $Y = Y_\infty$ to $Y = 0$, the effective conditions at the *fictitious* wall valid up to second order in ϵ read:

$$\hat{u}|_0 \approx \hat{\lambda}_x \left(\frac{\partial \hat{u}}{\partial \hat{y}} + \frac{\partial \hat{v}}{\partial \hat{x}} \right)\Bigg|_0 + \frac{\hat{\mathcal{K}}_{xy}^{itf}}{\mu} \frac{\partial}{\partial \hat{x}} \left(-\hat{p} + 2\mu \frac{\partial \hat{v}}{\partial \hat{y}} \right)\Bigg|_0 , \tag{4.37}$$

$$\hat{v}|_0 \approx -\hat{\mathcal{K}}_{xy}^{itf} \frac{\partial}{\partial \hat{x}} \left(\frac{\partial \hat{u}}{\partial \hat{y}} + \frac{\partial \hat{v}}{\partial \hat{x}} \right)\Bigg|_0 - \hat{\mathcal{K}}_{zy}^{itf} \frac{\partial}{\partial \hat{z}} \left(\frac{\partial \hat{w}}{\partial \hat{y}} + \frac{\partial \hat{v}}{\partial \hat{z}} \right)\Bigg|_0 , \tag{4.38}$$

$$\hat{w}|_0 \approx \hat{\lambda}_z \left(\frac{\partial \hat{w}}{\partial \hat{y}} + \frac{\partial \hat{v}}{\partial \hat{z}} \right)\Bigg|_0 + \frac{\hat{\mathcal{K}}_{zy}^{itf}}{\mu} \frac{\partial}{\partial \hat{z}} \left(-\hat{p} + 2\mu \frac{\partial \hat{v}}{\partial \hat{y}} \right)\Bigg|_0 . \tag{4.39}$$

The new parameters of the boundary conditions, $\hat{\lambda}_x$, $\hat{\lambda}_z$, $\hat{K}_{xy}^{itf}$, and $\hat{K}_{zy}^{itf}$, correspond to auxiliary variables that come from asymptotic analysis.

It is important to emphasize that these coefficients are not empirical, but arise from the solution of auxiliary systems of equations solved in the $\hat{x}$- or $\hat{z}$-periodic elementary cell. In particular, $\hat{\lambda}_x$ and $\hat{\lambda}_z$ are the components of the Navier-slip vector $\hat{\boldsymbol{\lambda}} = (\hat{\lambda}_x, 0, \hat{\lambda}_z)$, also called the effective slip length. The two terms, $\hat{K}_{xy}^{itf}$ and $\hat{K}_{zy}^{itf}$, are defined as interface permeabilities since, in analogy to Darcy's law in the bulk of the porous domain, they multiply the streamwise and spanwise gradients of the pressure in the expressions of $\hat{u}|_0$ and $\hat{w}|_0$. However, they differ from the corresponding intrinsic permeability components since, near the porous/free-fluid interface, grains are not as closely packed as in the bulk.

The auxiliary variables $(\hat{\lambda}_x, \hat{\lambda}_z, \hat{K}_{xy}^{itf}, \hat{K}_{zy}^{itf})$ are homogeneous to, respectively, a length and a surface area, and correspond to the product of their dimensionless counterparts times l and l^2:

$$\begin{aligned} \hat{\lambda}_x &= \lambda_x l, \\ \hat{\lambda}_z &= \lambda_z l, \\ \hat{K}_{xy}^{itf} &= K_{xy}^{itf} l^2, \\ \hat{K}_{zy}^{itf} &= K_{zy}^{itf} l^2. \end{aligned} \tag{4.40}$$

These coefficients are intrinsic to the geometric characteristics of the boundary and do not depend on the Reynolds number.

It is important to stress the fact that the first terms in the slip velocity components ($\hat{u}|_0$ and $\hat{w}|_0$), i.e. those containing the slip lengths $\hat{\lambda}_x$ and $\hat{\lambda}_z$, are of order ϵ, while all the other terms are of order ϵ^2. In the isotropic case we have $\hat{\lambda} = \hat{\lambda}_x = \hat{\lambda}_z$ and $\hat{\mathcal{K}}^{itf} = \hat{\mathcal{K}}_{xy}^{itf} = \hat{\mathcal{K}}_{zy}^{itf}$ so that the equations above can be simplified as:

$$\hat{u}|_0 \approx \hat{\lambda} \left(\frac{\partial \hat{u}}{\partial \hat{y}} + \frac{\partial \hat{v}}{\partial \hat{x}} \right)\Bigg|_0 + \frac{\hat{\mathcal{K}}^{itf}}{\mu} \frac{\partial}{\partial \hat{x}} \left(-\hat{p} + 2\mu \frac{\partial \hat{v}}{\partial \hat{y}} \right)\Bigg|_0 , \tag{4.41}$$

$$\hat{v}|_0 \approx \frac{\hat{\mathcal{K}}^{itf}}{\tilde{\lambda}} \frac{\partial \tilde{v}}{\partial \hat{y}}\Bigg|_0 , \tag{4.42}$$

$$\hat{w}|_0 \approx \hat{\lambda}\left(\frac{\partial \hat{w}}{\partial \hat{y}} + \frac{\partial \hat{v}}{\partial \hat{z}}\right)\Bigg|_0 + \frac{\hat{\mathcal{K}}^{itf}}{\mu}\frac{\partial}{\partial \hat{z}}\left(-\hat{p} + 2\mu\frac{\partial \hat{v}}{\partial \hat{y}}\right)\Bigg|_0 . \tag{4.43}$$

The purpose of our study is to correlate Hama's roughness function ΔU^+ to the slip length $\hat{\lambda}$ and to the vertical penetration distance $\dfrac{\hat{\mathcal{K}}^{itf}}{\hat{\lambda}}$, both measured in wall units.

4.4 Analytical construction of ΔU^+ from homogenized coefficients

The roughness function ΔU^+ represents a downward shift of the logarithmic velocity profile compared to the smooth-wall case, caused by the presence of surface roughness. Historically, it has been obtained through empirical correlations based on experimental measurements, as in the well-known Hama formulation. While this approach has been effective, it is limited to geometries similar to those tested experimentally and does not offer predictive capability for engineered or irregular surfaces.

The method adopted in this work, based on asymptotic homogenization theory, provides a systematic and generalizable way to construct an analytical formulation of ΔU^+, relying on λ_x and K_{xy}^{itf},computed from a microscale simulation over a representative periodic cell. By analogy with the classical logarithmic structure proposed by Hama, one can construct a predictive formula for ΔU^+ of the form:

$$\Delta U^+ = \frac{1}{\kappa}\ln\left(1 + a\lambda_x + b\sqrt{K_{xy}^{itf}}\right)$$

Where a and b represent the relative weight of the two homogenized parameters. These coefficients are calibrated by comparing the analytical prediction of ΔU^+ with data obtained from high-fidelity Direct Numerical Simulations (DNS). Specifically, for each roughness geometry considered, the following steps are carried out:

1. Compute λ_x and K_{xy}^{itf} from steady laminar simulations (e.g., via asymptotic homogenization);
2. Measure or retrieve ΔU^+ from DNS of turbulent flow over the same surface;
3. Fit the analytical expression by adjusting a and b to minimize the difference between predicted and DNS values of ΔU^+ (e.g., using least-squares regression).

Once this calibration is completed for a given class of rough surfaces, the values of a and b are held fixed. This is possible because all geometric information is embedded in the homogenized coefficients λ_x and K_{xy}^{itf}, and the analytical structure of the model remains valid across varying flow conditions. The resulting formulation becomes a predictive tool, no longer requiring empirical tuning for each new simulation.

Although not explicitly present in literature, this formula is dimensionally consistent, physically justified, and compatible with the logarithmic nature of velocity profiles observed in wall-bounded turbulence. It represents a natural extension of classical

roughness models, replacing empirical roughness heights k_s^+ with effective, homogenized quantities that capture the influence of geometry through first-principles analysis.

5 Modelling and Simulation of flow over rough surface

Numerical simulations of laminar flow were performed to evaluate slip parameters λ_x and K_{xy}^{itf} on a rough surface, represented by a layer of spheres, using water as a working fluid.

5.1 CFD software

STAR-CCM+ by CD-Adapco is the software we used for the simulations. STAR-CCM+ is a computational fluid dynamics software that enables to simulate multi-physics systems that operate in real conditions, in both 2D and 3D.
To run a simulation on this software, the following steps need to be performed:

- Definition of all the parameters and field functions;
- Design of the geometry of the problem;
- Set up of the boundary conditions for the domain;
- Mesh generation;
- Visualization and analysis of the results.

5.2 Geometry and Mesh Description

To simulate the behavior of laminar flow over a rough surface, a three-dimensional computational domain was designed, representing a periodic unit cell. The base of the cell is a square with side length $l = 1$, equal to the diameter of a hollow hemisphere embedded in the lower part of the domain. The hemisphere models the roughness element. This choice was also dictated by the possibility of comparing the results obtained with the values deriving from Nikuradse's experiments.

The domain is vertically divided into two regions:

- **Refinement region**: the lower zone between the *base wall* and the *interface-i*, which contains the hemispherical cavity. A finer mesh is used here to accurately capture slip effects and high viscous gradients near the rough surface.
- **Upper region**: the portion of the domain between *interface-i* and the *top surface*, representing the overlying fluid and completing the periodic cell.

The lateral surfaces of the domain are treated with **periodic boundary conditions** to simulate an infinitely repeating system in the horizontal plane. The interface between the two regions is defined as continuous.

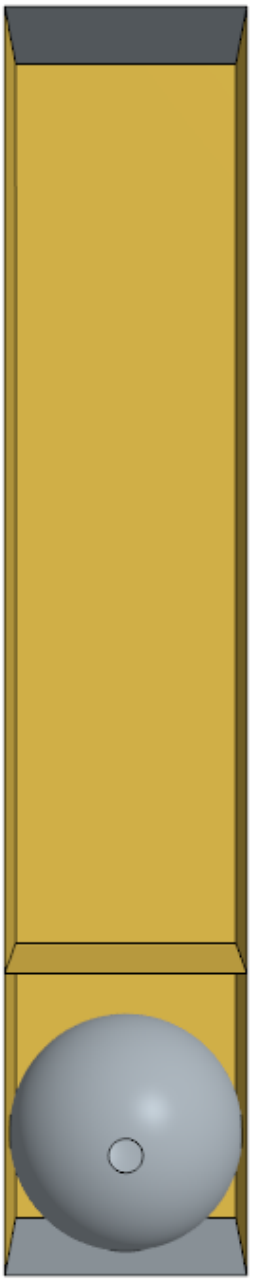

Figure 5.1: Geometry of the computational domain.

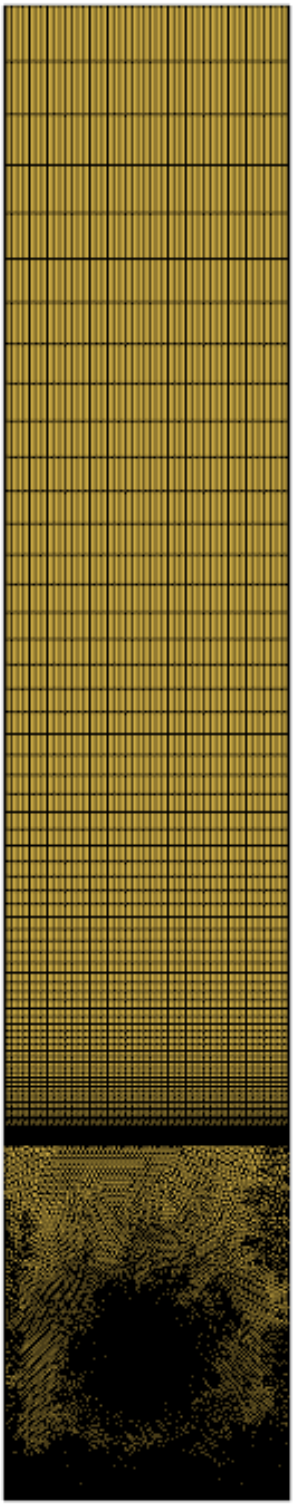

Figure 5.2: Mesh of the entire domain.

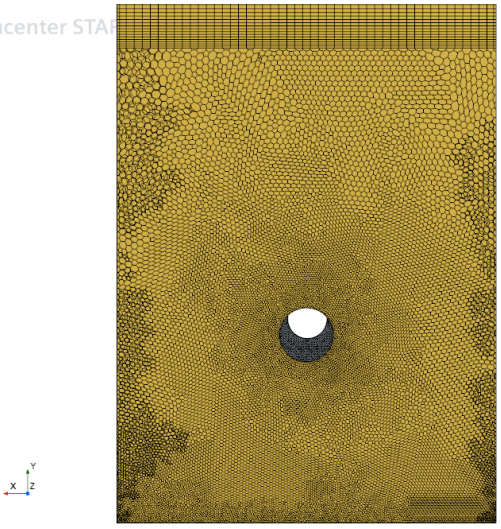

Figure 5.3: Lower part of the domain with a finer mesh. The hole is due to the sphere which is tangent to the cell layers.

More details of the mesh refinement strategy are explained in Chapter 6.2.

5.3 Boundary Conditions and Problem Setup

Choice of Physical Models

The physical models activated in the CFD simulation were selected to reflect the simplifying assumptions of the theoretical framework and to ensure numerical efficiency, while maintaining physical fidelity in the near-wall region. The following is a rationale for each selected model:

- **Laminar flow model (Steady, Laminar)**
  Although the final application of homogenized boundary conditions may target turbulent flows, the present simulation focuses on a steady, laminar regime. This choice was made to isolate and study the intrinsic effect of surface roughness on flow, without the added complexity of turbulence modeling. The laminar assumption also aligns with the first-order asymptotic analysis, which is typically formulated under simplified flow conditions.
- **Segregated flow solver (Segregated Navier–Stokes equations)**
  A segregated solver was employed to independently solve the momentum and continuity equations. This approach reduces the computational cost and is appropriate for incompressible laminar flows where pressure–velocity coupling does not pose significant stability issues.
- **Incompressible fluid with constant properties (Constant Density, Liquid H_2O)**
  Water was used as the working fluid, modeled as incompressible and with constant density and viscosity. These assumptions are standard in many wall-bounded-flow problems and are compatible with the dimensionless formu-

lation used in asymptotic homogenization. Constant properties simplify the analysis and are sufficient to capture the effects of geometric texture on momentum transport.

- **Gradient evaluation (Gradients)**
  The evaluation of gradients for derived quantities was activated to improve the calculation of viscous shear stress, which is crucial near the wall where steep gradients are expected. This is particularly important for the accurate extraction of the slip and permeability coefficients.

- **Three-dimensional model (3D)**
  A three-dimensional domain was essential to fully capture the spatial complexity introduced by the hemispherical cavity and to correctly resolve the three components of velocity and stress. This is in line with the theoretical derivation, which considers all directions in the formulation of effective boundary conditions.

- **Solution interpolation (Solution Interpolation)**
  This option was enabled to enhance numerical convergence, especially in regions with complex geometry and fine mesh, such as the roughness cavity. Interpolation contributes to the achievement of a stable and accurate solution.

These modeling choices reflect a compromise between physical accuracy and computational efficiency. They are consistent with the objective of characterizing the microscale flow field and extracting effective macroscopic parameters that can later be used in more complex, turbulent simulations.

Boundary Conditions

The choice of boundary conditions was made to be fully consistent with the multiscale homogenization theory, which assumes a periodic microscale structure and well-separated length scales. Below is a justification for each imposed boundary condition:

- **Top surface: prescribed constant velocity**
  A uniform velocity was imposed on the top surface of the computational domain. This ensures the presence of a well-defined shear flow across the height of the domain and allows the velocity profile to develop in response to the presence of the roughness elements below. Since the goal of the study is to investigate the effect of surface texture rather than to reproduce a specific experimental flow, prescribing the top velocity allows better control over the input conditions.

- **Bottom wall: no-slip condition on the rough surface**
  A no-slip condition was applied at the physical wall, including the hemispherical cavity. This accurately models the microscopic boundary, where the fluid adheres entirely to the solid surface. In the context of homogenization theory, this setup allows for the computation of effective slip and permeability parameters, which emerge as a result of the multiscale analysis applied to a strictly

no-slip microscale model.

- **Lateral surfaces: periodic boundary conditions**
  Periodic boundary conditions were applied on the lateral faces of the domain to represent an infinite repetition of the unit cell in the horizontal directions. This reflects the assumption of spatial periodicity at the microscale and avoids edge effects that could bias the solution. These conditions are essential to ensure that the domain functions as a representative elementary volume (REV) of an extended rough surface.

- **Interface between lower and upper regions: continuity condition**
  The virtual interface between the refined region containing the roughness and the upper bulk region was defined as continuous in both velocity and stress. This is consistent with the matching conditions used in asymptotic homogenization, where the microscale velocity and traction vectors must be continuous across the interface. This interface acts as the fictitious plane on which the effective boundary conditions are ultimately imposed.

This setup ensures that the simulation is both physically representative and mathematically well posed. It allows for the extraction of effective macroscopic quantities without resolving the entire wall-bounded turbulent flow, significantly reducing computational cost.

The decision to perform a *laminar steady-state* simulation, rather than a turbulent or time-dependent one, is also strategic. It provides a first validation step for the theoretical framework and allows for accurate computation of the auxiliary variables needed to define the slip length and permeability. These parameters can later be used in more complex simulations, including DNS, to model turbulent flows over textured surfaces more efficiently.

6 Conclusions

The main objective of this study was to investigate the relationship between surface roughness and its effects on turbulent flow, by employing the theoretical framework of asymptotic homogenization.

6.1 Visualization of Pressure and Velocity Fields

Qualitative analysis of the flow was performed by visualizing dimensionless fields in characteristic sections of the domain. The results highlight the influence of the rough surface on local pressure and velocity distributions.

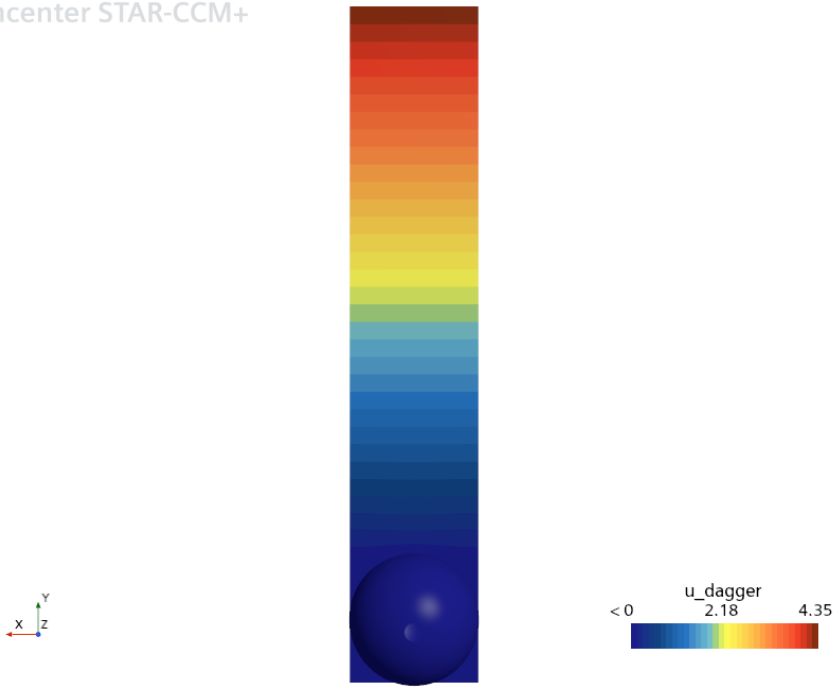

Figure 6.1: Dimensionless horizontal velocity field $u^{\dagger}$.

The velocity is zero on the hemispherical surface due to the no-slip boundary condition, and it gradually increases in the vertical direction, reaching its maximum at the top of the domain where the flow is fully developed. This trend is consistent with the expected laminar shear profile.

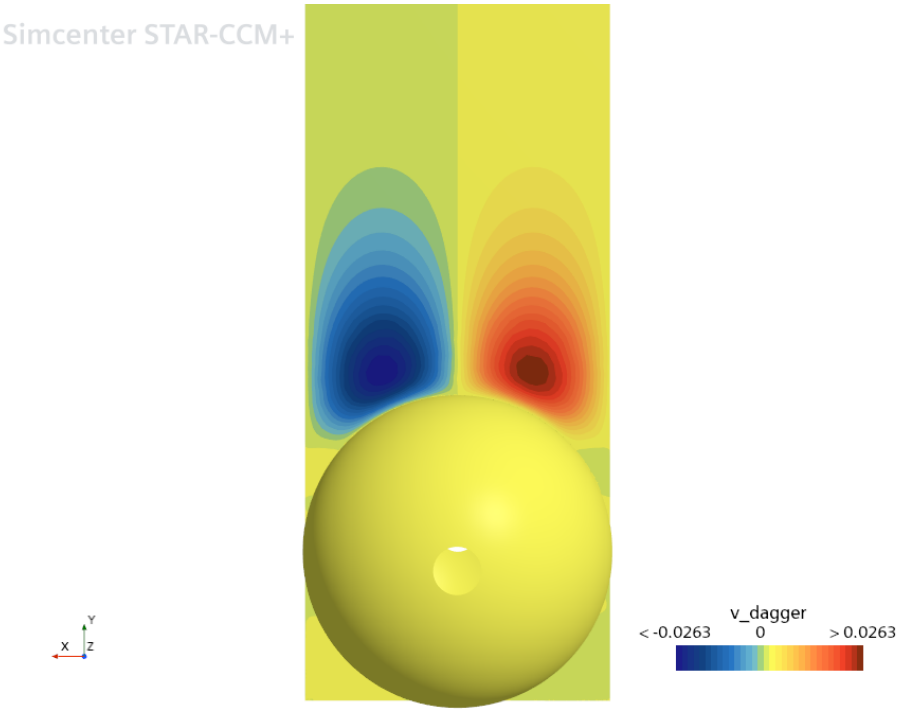

Figure 6.2: Dimensionless vertical velocity field $v^{\dagger}$.

The field shows small vertical displacements caused by the interaction of the flow with the cavity created by the sphere. The slight difference in color between the left and right halves of the domain suggests that the simulation may not have fully converged to a symmetric solution, possibly due to residual numerical imbalances.

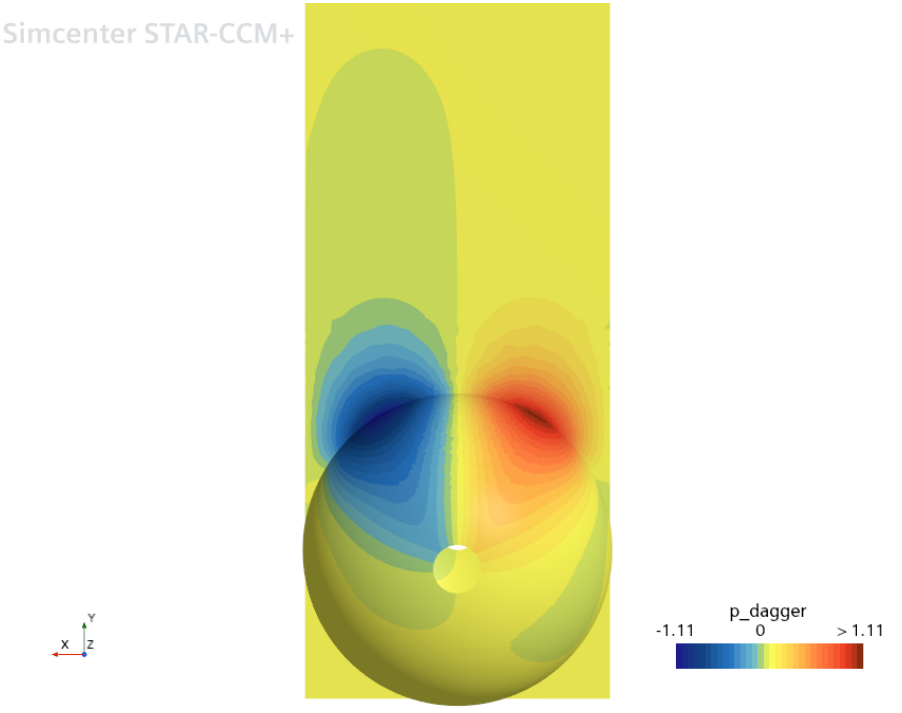

Figure 6.3: Dimensionless pressure field $p^{\dagger}$.

The pressure distribution highlights a lower pressure region inside the cavity. As with the vertical velocity, the slight asymmetry between the two halves of the domain may indicate that the solution did not reach full numerical convergence.

6.2 Numerical results

Through CFD simulations carried out on a representative three-dimensional geometry, it was possible to compute two key macroscopic parameters:

- **Slip length in the streamwise direction:** $\lambda_x = 0.1034$

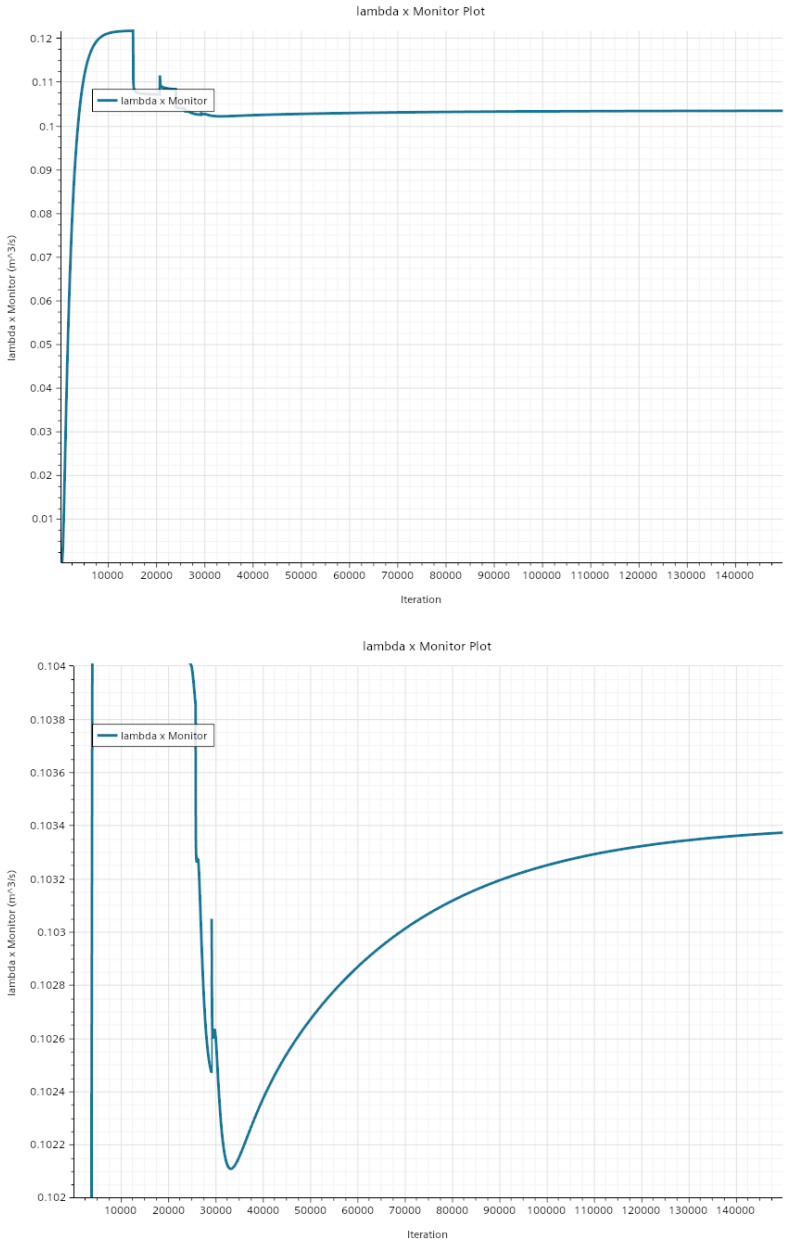

Figure 6.4: Convergence graphs of λ_x

- **Interfacial permeability in the xy direction:** $K_{xy}^{itf} = 0.0084$

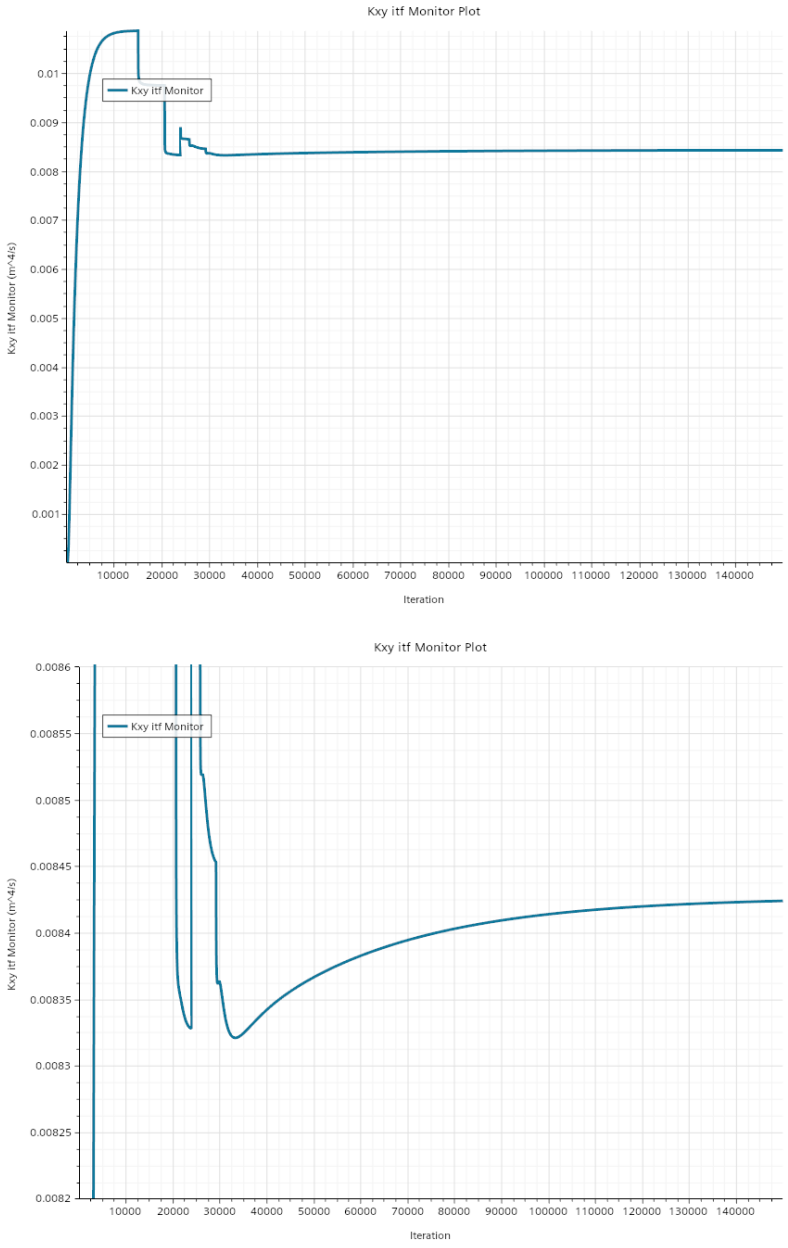

Figure 6.5: Convergence graphs of K_{xy}^{itf}

The convergence plots shown in Figures 6.4 and 6.5 illustrate the iterative evolution of the computed values for the slip length λ_x and the interfacial permeability K_{xy}^{itf} during the CFD simulation.

In the case of the **slip length** λ_x, the curve shows a rapid stabilization after a relatively small number of iterations. This behavior indicates that the tangential velocity field near the rough surface reaches a steady state quickly and that the horizontal component of the solution is well resolved. The smooth convergence of λ_x confirms the

reliability of the extracted value and suggests that it accurately reflects the geometric and physical configuration of the modeled surface.

For the **interfacial permeability** K_{xy}^{itf}, the plot also shows a tendency toward convergence, although with slightly more variation in the early iterations. This could be attributed to the greater sensitivity of the vertical flow (penetrating the roughness cavity) to small numerical imbalances or pressure field inaccuracies.

It is also worth noting that the **discrete jumps** observed in both curves are due to *mesh refinement operations* performed during the simulation. As the mesh becomes progressively finer, particularly in regions of high velocity or pressure gradients, the local numerical accuracy improves, and this can lead to sudden updates in the estimated values of λ_x and K_{xy}^{itf}. These adjustments are typical in simulations involving adaptive or manually refined meshes and are not indicative of instability but rather of increased resolution of microscale effects.

Instead of starting the simulation with the final, highly refined mesh, a progressive mesh refinement strategy was adopted. This approach offers several advantages in terms of numerical stability, convergence behavior, and computational efficiency.

Using a highly refined mesh from the very beginning of the simulation can lead to several issues:

- **Increased computational cost:** Fine meshes contain a large number of cells, which significantly increases memory usage and computation time, especially during early iterations when the solution is still far from convergence.
- **Numerical instability:** Solving the Navier–Stokes equations on a fine mesh with a poor initial guess can lead to divergence or oscillatory behavior in the solver. Starting with a coarser mesh and progressively refining allows the solver to build a better approximation of the solution step by step.
- **Improved convergence:** Gradual refinement helps reduce residuals (Fig. 6.6) and allows for a smoother convergence trajectory, as the solver adapts to increasingly accurate flow structures. This is particularly important in regions with strong gradients, such as around the roughness cavity.

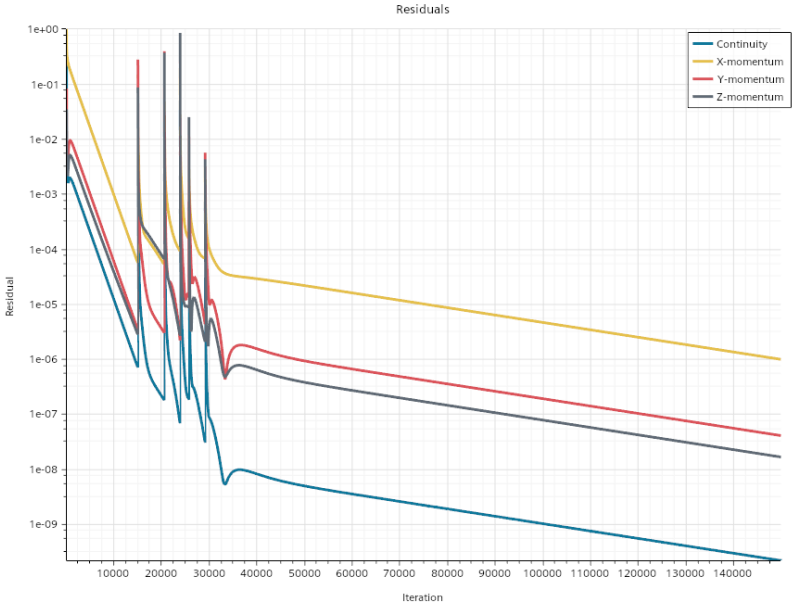

Figure 6.6: The residual represents the local error between the actual value of the solution and the value it should have if the equations were satisfied perfectly.

In this simulation, the refinement was focused particularly in the lower region of the domain, around the hemispherical cavity, where viscous effects and velocity gradients are more intense. The mesh refinement improves the local resolution in these critical zones, leading to more accurate estimates of the slip and permeability coefficients.

Although this strategy introduces slight discontinuities (or "jumps") in the convergence curves, it ultimately leads to a more stable and reliable solution. These jumps correspond to mesh updates and should be interpreted as signs of increased numerical precision rather than inconsistencies.

In summary, both graphs confirm that the simulation achieved good *numerical convergence*, which is essential for the reliability of the extracted parameters. These results validate the accuracy of the computational setup and support the use of λ_x and K_{xy}^{itf} within the asymptotic homogenization framework described in the earlier chapters.

These values provide an effective macroscopic description of the microscale behavior induced by surface roughness. In particular, the *slip length* quantifies how much the fluid appears to slip over the rough surface compared to a perfectly smooth one. The *interfacial permeability*, instead, expresses the extent to which the roughness allows vertical fluid penetration, affecting local pressure gradients and momentum exchange.

6.2.1 Importance of λ_x and K_{xy}^{itf}

The knowledge of these parameters proves to be extremely useful for several reasons:

- **Reduction in computational complexity:** Instead of resolving the detailed geometry of the roughness, the wall can be modeled using effective boundary conditions, significantly reducing the mesh size and computational cost.
- **Prediction and optimization:** The extracted coefficients allow one to evaluate and compare the effectiveness of different surfaces in reducing drag or improving heat and mass transfer.
- **Engineering applications:** These tools are valuable in the design of surfaces for aerodynamic, naval, HVAC (Heating, Ventilation, and Air Conditioning), biomedical applications and any context in which fluid structure interaction is involved.

In conclusion, the theoretical–numerical approach based on homogenization theory proves to be a powerful and versatile strategy for advanced flow modeling on complex surfaces. It is capable of producing coherent, interpretable, and reusable results for real-world engineering problems.

7 Future research developments

7.1 DNS Implementation Using Homogenization Parameters

Building on the results obtained from the present study, several directions can be taken to deepen the understanding of roughness-induced flow phenomena and to validate the asymptotic homogenization framework in more realistic turbulent conditions.
One of the most promising future developments consists in performing a **Direct Numerical Simulation (DNS)** of turbulent flow over the same rough surface. Unlike the current laminar steady-state simulation performed with CFD, which models flow behavior using simplified assumptions and effective boundary conditions, DNS fully resolves all the temporal and spatial scales of turbulence without any turbulence modeling.

The key differences between the two approaches are as follows:

- **CFD (current approach)**: Steady-laminar simulation with simplified physical models (e.g., constant density, no turbulence model); provides averaged or filtered results at low Reynolds numbers.
- **DNS (proposed)**: Fully transient, three-dimensional simulation that captures the complete spectrum of turbulent structures; significantly more accurate but extremely computationally expensive.

Using the slip length λ_x and the interfacial permeability K_{xy}^{itf} obtained in this work as inputs for the modeling of boundary condition or as validation parameters, DNS could help:

- Verify the consistency between homogenized models and resolved turbulence data;
- Refine the effective boundary conditions at higher Reynolds numbers;
- Validate the proposed empirical law for ΔU^+ and obtain the coefficients **a** and **b**.
- Compare the results with those obtainable through empirical methods

7.2 Alternative Surface Geometry: Hexagonal Packing

Another interesting research direction involves modifying the surface topology by changing the distribution of the roughness elements. In the present configuration, the rough surface consists of hemispheres arranged in a square-packed pattern, with one sphere per unit cell. An alternative proposed is to implement a **hexagonal packing of the spherical elements**.

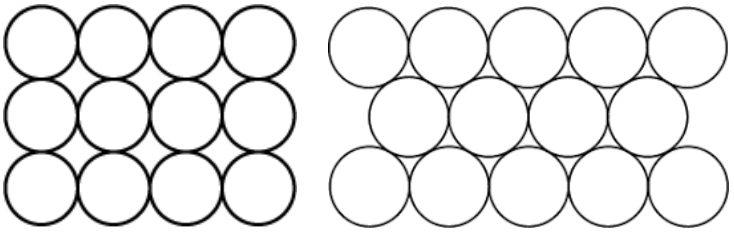

Figure 7.1: Difference between the two provisions

Hexagonal arrangements are known to offer more compact configurations and can influence the effective slip and permeability coefficients due to reduced interstitial spacing and altered shear-layer development. This change in geometry may yield the following results:

- Different values of λ_x and K_{xy}^{itf} due to altered flow recirculation patterns;
- Enhanced anisotropy effects in the velocity and stress fields;
- Potential drag reduction or enhancement depending on the configuration.

Simulating such a configuration, both in laminar and turbulent regimes, would contribute to a more complete understanding of how surface texture and packing density influence macroscopic flow behavior. Furthermore, it may help design optimized rough surfaces for specific engineering goals, such as heat transfer enhancement or drag minimization.

The proposed developments would bring this research closer to practical and industrial relevance by validating theoretical predictions through high-fidelity simulations and by exploring geometries that more closely resemble engineered surfaces.

References

[1] A. Salama. Velocity profile representation for fully developed turbulent flows in pipes: A modified power law. *Fluids*, 6(10):369, 2021.

[2] Y.A. Çengel and J.M.Cimbala. *Fluid Mechanics: Fundamentals and Applications*. Mc Graw Hill, 2009.

[3] A.J.Smits. *Lectures in Fluid Mechanics, Viscous Flows and Turbulence.* Princeton University, 2009.

[4] M. Kadivar, D. Tormey, and G. McGranaghan. A review on turbulent flow over rough surfaces: Fundamentals and theories. *International Journal of Thermofluids*, 10:77–100, 2021.

[5] K.A. Flack and M.P. Schultz. Roughness effects on wall-bounded turbulent flows. *Physics of Fluids*, 26:101–305, 2014.

[6] M. Thakkar, A. Busse, and N.D. Sandham. Direct numerical simulation of turbulent channel flow over a surrogate for Nikuradse-type roughness. *Journal of Fluid Mechanics*, 837, 2017.

[7] Misarah Abdelaziz, L. Djenidi, Mergen H. Ghayesh, and Rey Chin. On predictive models for the equivalent sand grain roughness for wall-bounded turbulent flows. *Physics of Fluids*, 36, 2023.

[8] Essam Nabil Ahmed and Alessandro Bottaro. Exploring the nexus among roughness function, apparent slip velocity and upscaling coefficients for turbulence over porous/textured walls. *Under consideration for publication in J. Fluid Mech.*, 2024.

[9] A Naqvi, S.B. Bottaro. Interfacial conditions between a free-fluid region and a porous medium. *Int. J. Multiph. Flow*, 2021.

[10] Naqvi S.B. Buda L. Bottaro A Ahmed, E.N. A homogenization approach for turbulent channel flows over porous substrates: Formulation and implementation of effective boundary condition. *Fluids*, 2022.